Research on the evolution mechanism of shale mechanical properties under variable bedding angles

Feng Du[1,2,3], Bing Liang[4], Xiaoyong Wen[5,6], Qian Liu[5,6], Junxiu Ma[7], Yixing Ren[8], Mi Zhang[9], Jihan Liu[10] and Jin Tan[8]*

[1]College of Mining, Liaoning Technical University, Fuxin, China, [2]China Coal Technology and Engineering Group Shenyang Research Institute, Fushun, China, [3]State Key Laboratory of Coal Mine Safety Technology, Fushun, China, [4]School of Mechanics and Engineering, Liaoning Technical University, Fuxin, China, [5]Oil & Gas Technology Research Institute of Changqing Oilfield Company, Xi'an, China, [6]State Engineering Laboratory for Exploration and Development of low-Permeability Oil and gas fields, Xi'an, China, [7]Oil Production Technology Research Institute, PetroChina Xinjiang Oilfield Company, Karamay, China, [8]School of Civil Engineering and Geomatics, Southwest Petroleum University, Chengdu, Sichuan, China, [9]CNPC Offshore Engineering Company Limited, Beijing, China, [10]School of Geodesy and Geomatics, Wuhan University, Wuhan, Hubei, China

Mechanical properties are significantly influenced by highly developed bedding planes in shales. This leads to incorrect prediction of fracturing parameters, which results in inefficient fracturing reconstruction of shale reservoir. Therefore, it is of great significance to investigate the effect of bedding planes on the mechanical properties of shales and the mechanism of fracturing efficiency. In this paper, uniaxial compression experiments under variable bedding angles are carried out based on the outcrop shale of the Longmaxi Formation in Sichuan, China. Thereafter, the Aramis system is employed to examine the deterioration process and morphology of the specimens, and the Mechanical properties obtained are utilized to investigate the mechanisms through which the bedding plane influences the hydraulic fracturing stimulation. The findings of the study indicate that the compressive strength and modulus of elasticity of the specimens initially decrease and then increase with an increase in bedding angle. When the bedding angle at the range of 0°−15°, the predominant failure mode observed in the specimens is a mixed failure involving tension and shear, which penetrates the bedding plane. The failure mode observed in the specimen, with a bedding angle of 30°−60°, is predominantly shear failure along the bedding plane. In specimens subjected to a bedding angle of 75°−90°, failure modes are typically tensile failure parallel to the bedding plane and shear failure along the bedding plane. During hydraulic fracturing, the initial expansion of fractures occurs in a direction perpendicular to the minimum horizontal principal stress. In the event that the model contains bedding planes, the hydraulic fracture tends to expand along the bedding plane following an intersection with the plane. This phenomenon serves to promote a significant extension of the hydraulic fracture. Furthermore, the model incorporating bedding planes exhibits reduced apertures of hydraulic fractures and diminished pressures during the propagation stage of the fractures in comparison to the base model. The research results contribute to a comprehensive understanding of the evolutionary mechanisms governing the mechanical properties of shale

reservoirs, as well as the expansion patterns of fractures under hydraulic fracturing stimulation.

1 Introduction

The exploitation of shallow energy sources is resulting in their progressive depletion. In contrast, deep unconventional energy sources, which are characterized by their substantial reserves, are gradually becoming a more prominent focus (Liu H. et al., 2023; Tan et al., 2023; Wu et al., 2023). Shale gas, as a novel unconventional clean energy resource, exhibits several distinctive characteristics, including a deep burial depth, a relatively narrow pore throat radius (Li et al., 2020) (Zhang F. S. et al., 2022; Lin et al., 2024b), a developed reservoir bedding plane, and a complex structural composition (Huang et al., 2023a; Wu et al., 2023; Song et al., 2017). This situation gives rise to inefficiencies when hydraulic fracturing stimulation is carried out in shale gas reservoirs, which in turn restricts the commercial extraction of shale gas (He et al., 2017; Lin et al., 2017; Tan et al., 2024c). Consequently, it is of paramount importance to investigate the mechanical property evolution regulations of shale reservoirs under disparate bedding angles, with the objective of facilitating the extraction of deep shale gas.

The geologic history of shale reservoirs is characterized by a series of movements and external effects that occur during the deposition and compaction stages (Tan et al., 2024; Huang et al., 2025; Zhang et al., 2017). These processes may give rise to mineralization and mild metamorphism which changes their mineral composition and properties, resulting in varying sizes and uneven distribution of the mineral grains that make up the shale reservoir (Lin et al., 2024a; Tan et al., 2021; Song et al., 2020). This leads to notable anisotropy in the mechanical properties and damage mechanisms of shale reservoir (Zhu et al., 2024) (Huang et al., 2019; Tan et al., 2017; Huang et al., 2024a). In comparison to other rocks, shale reservoirs are characterized by a high density of bedding planes and joints, which exert a considerable influence on their mechanical properties (Zheng et al., 2022; Huang et al., 2022; Fu et al., 2024; Song et al., 2024). In this regard, Liu et al. conducted experiments based on laminated rock specimens using acoustic emission and digital image correlation uniaxial compression tests. The results demonstrated that the bedding plane had a considerable impact on the mechanical properties and fracture toughness of the specimens, and the lowest strengths and failure strains were predominantly observed at bedding angles of 30°–60°(Liu M. et al., 2023; Huang et al., 2024b). Furthermore, the AE hit rate, cumulative AE hit and cumulative AE energy indicate a decline followed by an increase with rising bedding angles (Liu Q. et al., 2023). Luo et al. employed the Brazilian splitting method to examine the tensile properties of anisotropic rock specimens under diverse bedding plane conditions. The experimental analysis revealed that the brittleness index of the specimens exhibited a gradual increase with the rise in bedding angle (Luo et al., 2023). In light of these

studies, Khalili proceeded to conduct compressive and three-point bending tests, which revealed that the maximum fracture load and fracture surface energy of the specimen tend to increase with an increase in bedding angle, and the mechanism of fracture extension underwent a transformation (Khalili et al., 2023). Zhai et al. employed a bonded particle model embedded with a moment tensor algorithm to investigate the progressive damage process of shale under uniaxial compression. Their findings revealed that shear failure facilitates progressive failure and the formation of a complex fracture network, which may enhance the efficacy of hydraulic fracturing stimulation of reservoirs (Zhai et al., 2022). Hydraulic fracturing represents a principal method of extracting shale gas by injecting a substantial volume of high-speed fracturing fluid into the target reservoir over a brief period (Ji et al., 2015; Song et al., 2022), with the objective of fracturing the reservoir and establishing a high-speed transmission channel between the reservoir and the wellbore (Zhang Y. et al., 2022; Huang et al., 2020). Given the prevalence of bedding planes in shale deposits, the stress generated by hydraulic fracturing during the reconstruction of shale reservoirs can result in the extension or displacement of bedding planes, thereby creating a network of complex fractures (Huang et al., 2023b; He et al., 2023; Huang et al., 2024b). In order to analyze the influence mechanism of bedding plane on hydraulic fracture extension, Zhang et al. established a fluid-solid coupling model based on the continuum-discontinuity element method. Their findings indicated that shear failure typically occurs when the fracture approaches the bedding plane (Zhang F. S. et al., 2022). Furthermore, the presence of the bedding plane impedes the growth of hydraulic fracture height, with the degree of impeding dependent on the mechanical properties of the bedding plane (Gu et al., 2024) (Zhang B. et al., 2024) (Zhang Y. et al., 2024). Nevertheless, the majority of extant studies are confined to two-dimensional or proposed three-dimensional analyses (Gao et al., 2024; Luo et al., 2022; Zeng et al., 2023; Liu et al., 2022), and the precise interaction mechanism between hydraulic fracture and bedding plane remains elusive.

Therefore, in order to investigate the influence of bedding angles on the mechanical behavior of shale, this study employs the preparation of shale specimens under different bedding angles. The specimens are then subjected to indoor uniaxial compression experiments, during which their damage process and morphology is analyzed and summarized using the Aramis system. The resulting data allows for the observation and characterization of the conventional damage morphology of shale, as well as the mechanism of fracture evolution. In addition, this paper employs a genuine three-dimensional strong hydro-mechanical coupling, constructed using the 3D discrete lattice method, to examine the impact of an inclined bedding plane on the morphology of hydraulic fractures.

2 Experimental design and methods

2.1 Experimental scheme design

The specimens examined in this study are derived from the outcrop shale of the Longmaxi Formation in Sichuan, where the bedding planes are markedly developed. The outcrop shale was sampled at the same location and without any obvious cracks to guarantee that the shale specimens used in the indoor testing had a high degree of integrity and were not substantially different. Additionally, the bedding plane of the outcrop shale must be clearly defined in order to facilitate the drilling of specimens with varying bedding angles. In this study, the bedding angle (α) is defined as the angle between the bedding plane and the end face of the cylindrical specimen. The specimens were drilled in accordance with the manner depicted in Figure 1. The left part of the figure illustrates a schematic representation of all the specimens that were drilled, while the right part of the figure displays the specimens with $\alpha =$ 0°, 15°, 30°, 45°, 60°, 75° and 90°. Following the drilling process, the samples were processed into standard samples with dimensions of 50 mm × 100 mm. A total of seven groups of shale specimens with varying bedding angles were processed, with three samples taken from each group, for a total of 21 samples. These samples were then grouped according to the bedding angle, from low to high. The measurements of specimen strain and displacement employed in this study are obtained through the tracking and monitoring of transverse and longitudinal displacement variations at disparate points on the specimen surface with the use of a high-definition dual camera. Prior to the commencement of the experiments, the shale specimens were subject to a spot spraying technique, ensuring that the dimensions of the sprayed areas are sufficiently small to allow for the formation of clear, fine, and randomly distributed spots on the surface of the specimens. To eliminate the potential for the top effect to impact the experimental results, the specimens are treated and lubricated prior to the indoor experiments.

2.2 Experimental methods of rock mechanics

In order to obtain the mechanical properties and fracture evolution of shale under uniaxial compression at different bedding
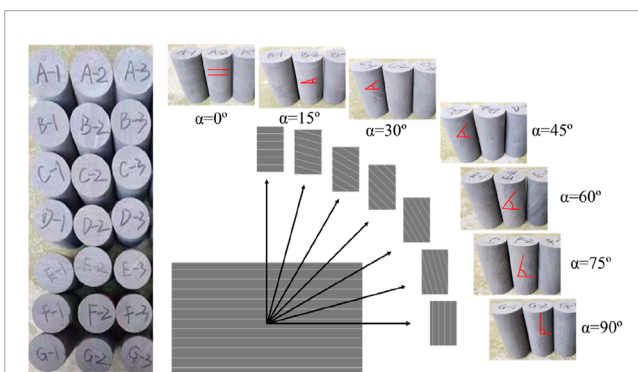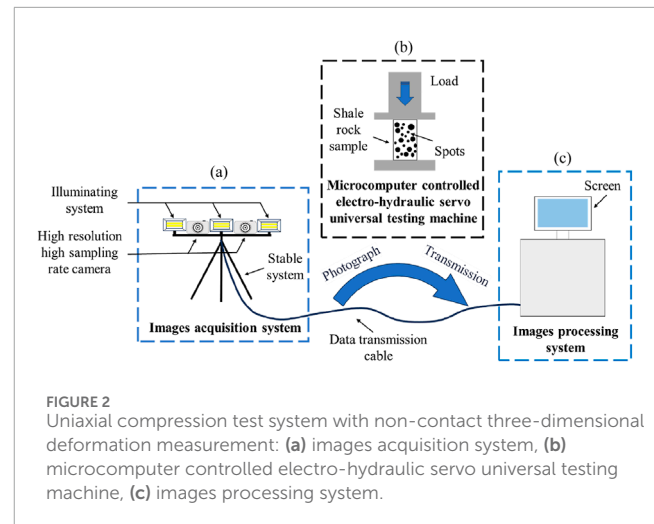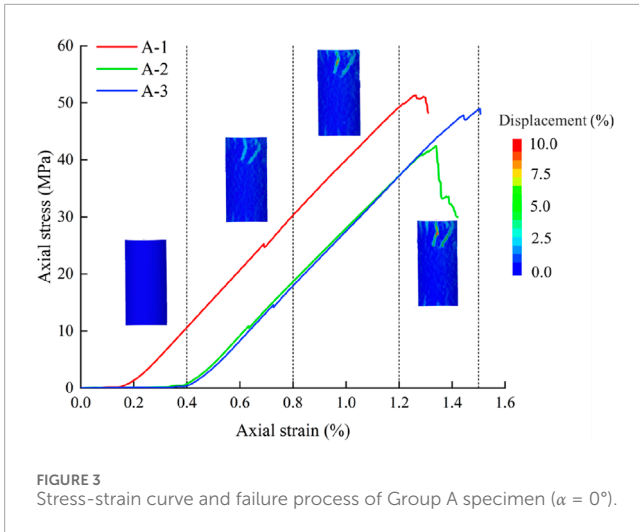
FIGURE 2
Uniaxial compression test system with non-contact three-dimensional deformation measurement: **(a)** images acquisition system, **(b)** microcomputer controlled electro-hydraulic servo universal testing machine, **(c)** images processing system.

angles, the uniaxial compression test system with non-contact three-dimensional deformation measurement is employed in this study. This allows for the acquisition of stress-strain curves of the rocks, as well as the tracking of deformation and failure processes of the surface of the rock specimens under uniaxial action. Furthermore, it enables the analysis of the evolution of the fracture of the rock specimens during deformation and failure. The indoor uniaxial compression test was conducted utilizing a microcomputer-controlled electro-hydraulic servo universal testing machine (Figure 2b), which is capable of applying a maximum pressure of 1,000 KN. During uniaxial loading of the specimen, the strain and deformation damage processes were observed using an Aramis graphic acquisition system (Figure 2a), which comprises two high-resolution, high-sampling-rate cameras (resolution 2,448 × 2050, acquisition rate 15 Hz) and an illumination system. The deformation damage processes were transmitted to the graphic system *via* transmission cables. The graphics processing system (Figure 2c) consists of a graphics workstation, a controller and a monitor to analyze the degree of deformation in different parts of the specimen and to record the fracture extension process in the specimen by means of the Aramis3D graphics processing software. The system is capable of measuring specimen sizes ranging from 1mm to 1000 mm with an accuracy of 0.01%, and measurement range extends from 0.01% to 500%. In the experiment, the universal experimental compressor employs a displacement-controlled loading mode, with a loading rate of 0.1 mm/min and a camera shooting speed of one picture/second. This allows for the comprehensive documentation of the specimen's deformation and subsequent destruction.

3 Experimental results and analysis

The failure patterns of rocks are typically classified into three main categories: split-tension failure, shear-slip failure, and composite failure patterns combining splitting and shearing (Shao et al., 2024; Fu et al., 2024). The α of the specimens in group A is 0°, and the deformation damage process of A-3 under axial load is shown in Figure 3. The experimental results reveal that the end of the specimen is the initial site of stress concentration

FIGURE 1
Specimen preparation and grouping.

FIGURE 3
Stress-strain curve and failure process of Group A specimen ($\alpha = 0°$).

FIGURE 4
The failure process of the specimen and the corresponding cloud diagram.

FIGURE 5
Stress-strain curve and failure process of Group B specimen ($\alpha = 15°$).

and the emergence of shear fractures. Subsequently, secondary fractures gradually develop in the specimen, extending in the axial direction and penetrating into the existing fractures at the end of the specimen. As the load was increased, the fractures in the specimen grew in length, ultimately leading to the specimen's complete collapse. This resulted in shear splitting mixed-mode damage, accompanied by a discernible anisotropy in the damage process.
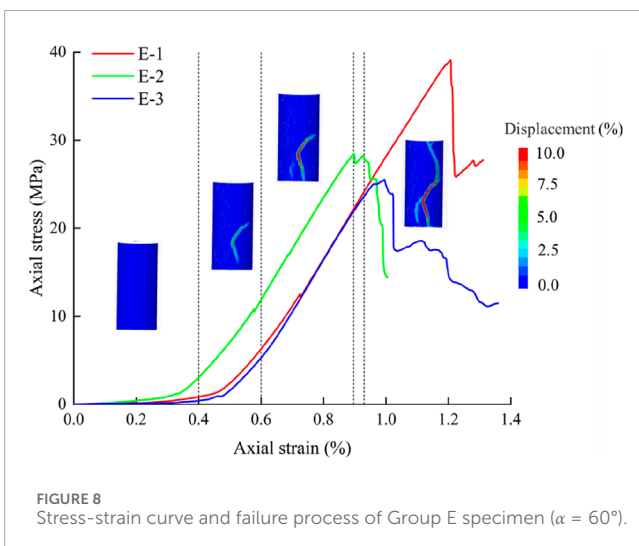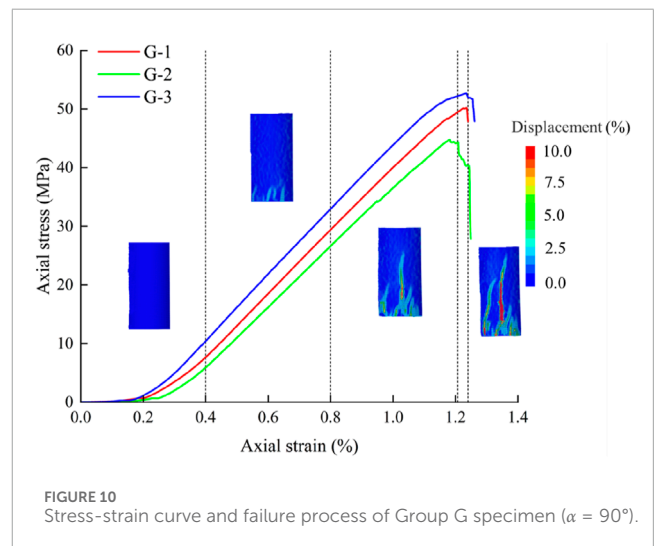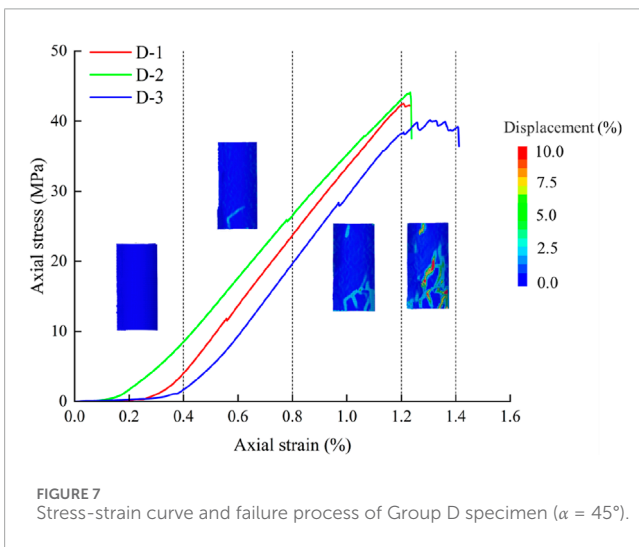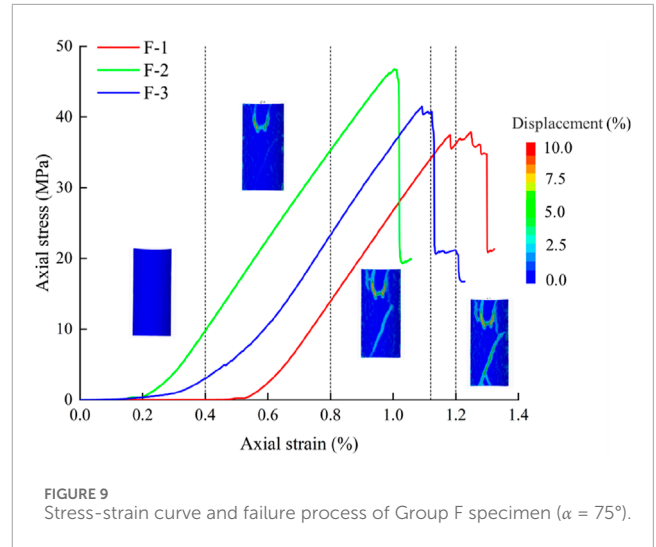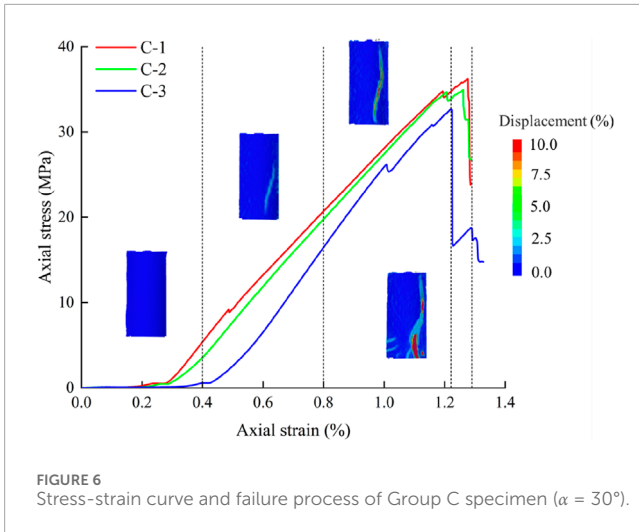
The stress-strain curves, plotted based on the uniaxial compression test data, demonstrate that the stress-strain curves of the specimens can be divided into four distinct stages: the compression-tightening stage, the elasticity stage, the yielding stage, and the destructive stage (Zhao et al., 2022), as shown in Figure 4. The micro-fissures and structural surfaces within the matrix in the compaction stage are gradually closed under external pressure. Additionally, the fractures expand stably in the elasticity stage, the stress-strain curve is almost straight and the stiffness of the specimen remains basically unchanged, at the same time, micro-fractures appear and begin to expand. The yield stage is characterized by the unstable development of the fracture, whereby an increase in load outside the rock results in a concentration of stress at the fractures and pores within the rock. This leads to a transformation in the fracture from stable extension to unstable extension, with the energy within the rock rapidly accumulating and the fracture developing rapidly into a macroscopic fracture. This process reaches its peak stress intensity at the critical energy release point. In damage stage, the overall structure of the specimen is compromised by the formation of complex fractures network. As the load continues, the fractures merge with one another, resulting in the formation of a macroscopic fracture surface. Concurrently, secondary fractures emerge, accompanied by an increase in fracturing and deformation displacement. This leads to the collapse of the specimen block or the complete failure of the specimen.

The stress-strain curve of Group B and the deformation and damage process of the B-2 shale specimen are shown in Figure 5, where the α is 15°. Defects, such as microfractures and bedding planes, which existed in the shale specimen, resulted in chipping of the edges of the specimen surface when subjected to loading. Fracturing occurred in B-2 at the upper end during the elastic phase, with expansion in the axial direction subsequently observed.
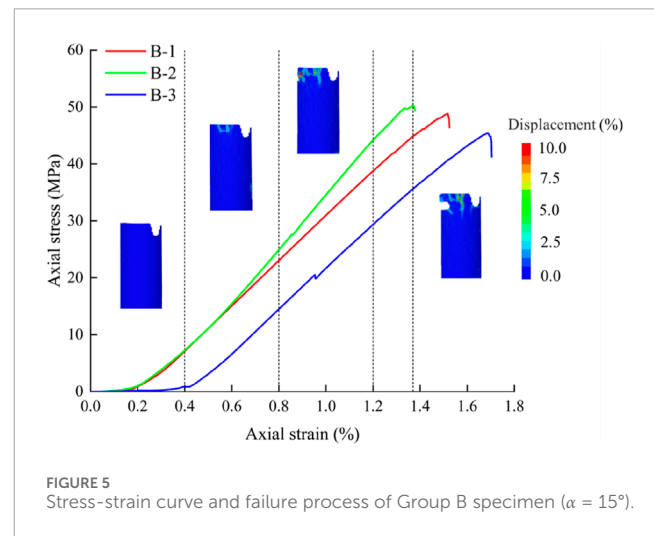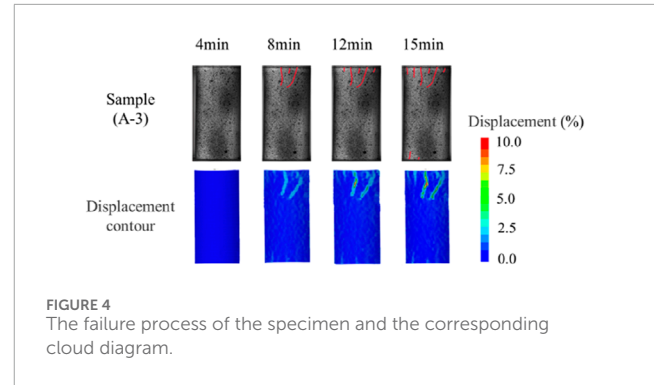
This was followed by gradual linking of these fractures with each other. Upon reaching a compressive axial strain of 1.2%, a notable deformation was observed in the upper left region of the specimen. As the applied load increased, the fracture in this area propagated and merged with the primary fracture, exceeding the bearing capacity of specimen and resulting in the formation of macroscopic fractures. Subsequently, the uniaxial compressive strength attained its maximum value, which was followed by the collapse of the upper-left section of the specimen, accompanied by a prevalence of mixed splitting-shear damage, predominantly splitting.

As illustrated in Figure 6, the stress-strain curve of the specimen at α of 30° is shown, along with the deformation damage process of specimen C-3. When subjected to axial pressure, the upper surface of the C-3 specimen exhibited peeling at the compaction stage, accompanied by fluctuations in the stress-strain curve. During the elastic stage, an inclined fracture emerged within the specimen and gradually expanded throughout, resulting in a notable reduction in the compressive strength of the specimen. The aperture of the fracture in the specimen further increases when the axial compression of the specimen reaches 1.3%, accompanied by the emergence of new fractures along the bedding plane on the left side. Additionally, new microfractures are generated below the main fracture, penetrating it and ultimately leading to the complete destruction. In comparison to the above damage process of the specimen, the expansion of the fractures was influenced by the

FIGURE 6
Stress-strain curve and failure process of Group C specimen (α = 30°).

FIGURE 9
Stress-strain curve and failure process of Group F specimen (α = 75°).

FIGURE 7
Stress-strain curve and failure process of Group D specimen (α = 45°).

FIGURE 10
Stress-strain curve and failure process of Group G specimen (α = 90°).

FIGURE 8
Stress-strain curve and failure process of Group E specimen (α = 60°).

bedding plane when the α was 30°. This caused a reduction in the uniaxial compressive strength of the specimen.

The stress-strain curve of the specimen in Group D, characterized by α of 45°, along with the deformation damage process of specimen D-3 under axial load, are depicted in Figure 7. In the elastic stage, shear fractures initially emerged at the inferior end of the specimen and deflected. Subsequently, the fractures commenced their propagation, while the left side of the specimen exhibited a tendency to disintegrate as a consequence of the intensification of fracture and stress. During the yielding stage, new fractures formed in the specimen, rapidly extending along the bedding plane and gradually penetrating the previously formed fractures, resulting in a more complex fracture morphology. In the damage stage, a substantial number of new fractures were generated along the bedding plane over time, resulting in the formation of a more intricate fracture network. This network was established through the communication between fractures under the influence of loading, and extended throughout the specimen, which subsequently led to the destruction of the specimens. In comparison to the specimens in Group C, the fracture extension

in Group D was markedly influenced by the bedding plane, with a greater propensity for new fractures to emerge between the bedding planes. Additionally, the number of fractures and their morphology were more intricate in Group D, and the damage to the specimens was more comprehensive.

As depicted in Figure 8, the stress-strain curves of the shale specimens at α of 60° are shown, along with the deformation damage process of the E-2 specimen. A partial extension of the fracture along the bedding plane was initially observed in the E-2 specimen, which exhibited a tendency to extend along the end of the specimen during the yielding stage. This phenomenon was accompanied by the emergence of new microfractures along the bedding plane, leading to a gradual reduction in the specimen's load-bearing capacity. As the load increases, the fracture in the specimen rapidly extends, continues to deflect at the upper end of the specimen, and propagates through the entire specimen. The macroscopic fractures in the specimen are primarily distributed along the bedding plane.

The stress-strain curve of the bedding plane in Group F with α of 75° and the deformation and damage process of the F-3 shale specimen are shown in Figure 9. The phenomenon of stress concentration initially occurred at the top of the specimen under axial loading, resulting in the formation of axial microfractures. During the yielding stage, new axial microfractures were generated at the top of the specimen, with the fractures subsequently connecting with each other to form a macroscopic fracture. Additionally, inclined fractures along the bedding plane were generated in the middle part of the specimen. As the axial load is increased, the fractures that extend along the bedding plane communicate with the macroscopic axial fractures at the top of the specimen, and subsequently propagate throughout the specimen.

As illustrated in Figure 10, when α is 90°, the stress-strain curve of specimen Group G and the deformation damage process

of specimen G-2 are depicted. The influence of the α was observed to result in a higher incidence of axial fracturing at the extremity of the specimen under axial load. During the loading process, the microfractures that were present in the edge region of the specimen underwent continuous compaction, resulting in an uneven distribution of stress. This led to the partial detachment of the edge region of the specimen. In the yielding stage, some of the fractures in the specimen rapidly expanded along the 90° bedding plane and gradually developed into macroscopic fractures, with the fractures subsequently connected with each other. This resulted in a reduction of the load-carrying capacity and a peak in the uniaxial compressive strength of the specimen, which was subsequently destroyed.

In this experiment, all specimens exhibited a notable increase in the sharpness of the curve and a considerable rise in the slope of the curve during the compaction stage. The analysis of the stress-strain curves at varying bedding angles revealed that the majority of the curves exhibited minor fluctuations in the elastic phase and pronounced deviations after the peak stress point. This indicates that the internal fractures in the specimens were consolidated during the loading process, subsequently influencing the load-bearing curve of the specimens. In some specimens, a double peak stress point is observed near the peak of the stress curve. This is characterized by a maximum in the bearing capacity of the sample, accompanied by a significant number of macroscopic fractures. These result in a reduction in bearing capacity and a redistribution of internal stresses. Subsequently, the overall structure of the sample is compromised, leading to a rapid decline in strength levels. Following the peak stress, the curve displays a segmental decline. This is accompanied by the formation of macro-fracture in the specimen, leading to significant alterations in the overall structure. These changes give rise to an accelerated reduction in the load-bearing capacity, accompanied by a redistribution of internal stress.
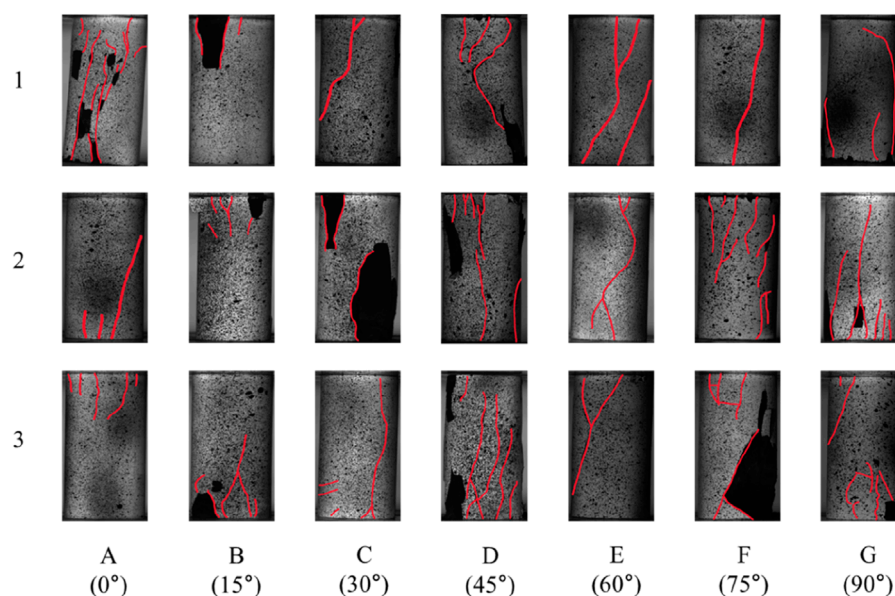

FIGURE 11
Failure mode of specimens. **(A)** 0°, **(B)** 15°, **(C)** 30°, **(D)** 45°, **(E)** 60°, **(F)** 75°, **(G)** 90°.

Ultimately, the load-bearing capacity is completely lost. In some instances, the fracture of the specimen occurs in a direct manner through the entirety of the specimen, resulting in the complete loss of its load-bearing capacity. In such cases, the curve displays a vertical decline or a complete disappearance.
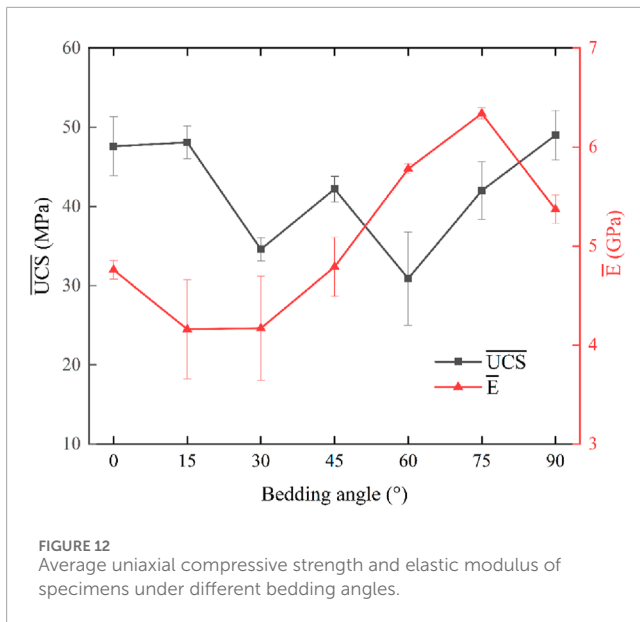
4 Discussion

4.1 Failure mode and mechanical properties of specimens

The deformation characteristics and mechanical strength of shale are inextricably linked to its damage pattern. Furthermore, the damage pattern of specimens tends to change with the α. By distinguishing and summarizing the damage patterns of all test specimens, as shown in Figure 11, the damage processes and damage patterns of the specimens are mainly classified into the following

three types. The first one is the tension-shear mixed damage mode through the bedding plane, which occurs in almost all test specimens. In this damage mode, the fracture first appears at the end of the specimen, and with the increasing load, the tensile or shear fracture continues to extend and then passes through the bedding plane to damage the overall structure of the rock sample; The second damage mode is tension damage, which occurs in parallel with the bedding plane. This phenomenon is most prevalent in specimens with high bedding angles. The parallel or small angle between the bedding plane and the loading direction, in conjunction with the weak mechanical properties between the bedding planes, causes the fracture to propagate along the bedding plane. Furthermore, the fractures at the extremities of the specimens interact with one another, leading to the emergence of shear fractures. The final type is shear damage along the bedding plane, which commonly occurs in specimens with a low bedding angle. The pattern and number of fractures are typically straightforward, with a single main fracture that shears along the bedding plane and traverses

TABLE 1 Mechanical properties of specimens with different bedding dip angles.

Sample	α(°)	UCS(MPa)	ε	E (GPa)	$\overline{UCS}$(MPa)	$\bar{\varepsilon}$	$\overline{E}$ (GPa)
A-1	0	51.30	1.31	4.85	47.6	1.38	4.76
A-2		42.50	1.34	4.63			
A-3		48.90	1.50	4.80			
B-1	15	48.80	1.51	3.95	48.1	1.52	4.16
B-2		50.20	1.37	4.86			
B-3		45.30	1.68	3.69			
C-1	30	36.20	1.27	3.71	34.6	1.25	4.17
C-2		34.90	1.26	3.87			
C-3		32.60	1.22	4.89			
D-1	45	42.50	1.20	4.93	42.2	1.24	4.79
D-2		44.00	1.23	4.38			
D-3		40.10	1.30	5.07			
E-1	60	39.10	1.20	5.73	30.9	1.02	5.78
E-2		28.40	0.89	5.77			
E-2		25.40	0.99	5.85			
F-1	75	37.80	1.24	6.34	42.0	1.11	6.34
F-2		46.70	1.00	6.27			
F-3		41.50	1.09	6.41			
G-1	90	50.20	1.23	5.43	49.0	1.20	5.37
G-2		44.70	1.18	5.21			
G-3		52.10	1.00	5.56			

FIGURE 12
Average uniaxial compressive strength and elastic modulus of specimens under different bedding angles.

the entire specimen, resulting in comprehensive structural damage. It can be seen that when the α is 0°~15°, the bedding angle is almost perpendicular to the loading direction, and the predominant damage mode observed in the specimen is a combination of tension and shear damage through the bedding plane. During the compression phase, the specimen exhibits a splitting and destructive behavior, forming a macroscopic fracture. Due to the low bedding angle and the low tensile stress, the fracture tends to penetrate the bedding plane and expand along the loading direction. As the α of the specimen is 30°~60°, it can be concluded that the predominant damage mode is shear damage along the surface of the bedding plane. In the compression test, the specimen initially exhibited microfractures that traversed the bedding plane, which influenced the distribution of stress within the specimen and consequently resulted in stress concentration. As the axial load increased, the stress between the bedding planes augmented, which prompted the microfractures to expand along the bedding plane and enabled the shear fractures to develop into the shear plane. In specimens subjected to α of 75°~90°, the predominant damage mode is tensile damage parallel to the bedding plane and shear damage along the bedding plane. Due to the relatively small angle between the loading direction and the α, the specimen initially produces microfractures along the bedding plane. These fractures subsequently expand along the bedding plane and gradually penetrate the end of the specimen during the loading process. This results in the formation of multiple tensile damage surfaces and shear damage surfaces. The failure morphology of each specimen group after the test is shown in Figure 11, and the black part of it is the part of the specimen that chipped off during the experiment. The red line indicates the fracture that formed on the surface of specimen, and the black part shows the area of the outer specimen surface that was destroyed as a result of chipping.

Through observation and analysis of the macroscopic destruction process and fracture morphology of the rock samples during the experiment, it was determined that the final destruction of the specimens was predominantly characterized by chipping

and fracturing, which resulted in the production of a considerable number of fragments or blocks. This suggests that the brittleness of shale is a more significant factor. Moreover, the experimental findings indicated that the greatest number of fractures was observed in specimens with α of around 45° and 90°. This was due to the fact that the shear stresses were aligned with the bedding plane at 45°, which resulted in an elevated number of fractures along the bedding plane. As a result, the specimens exhibited greater damage and more complex fracture patterns. In the case of α of 90°, the bedding plane were oriented in the same direction as the tensile stress. The lower mechanical strength of the bedding plane relative to the matrix resulted in a significant increase in the number of fractures in the specimens.

The average elastic modulus and compressive strength are pivotal parameters for the analysis of reservoir physical properties, which directly impact the critical pressure required for hydraulic fracture initiation as well as the extension trend of subsequent fractures. For instance, reservoirs with low modulus may encourage the formation of intricate fracture networks (e.g., bifurcation, steering, *etc.*) as a consequence of plastic deformation during reforming. Consequently, analyzing the evolution patterns of average modulus of elasticity and compressive strength with stratigraphic dip is a cornerstone for optimizing fracture morphology, controlling construction risks, and assessing the effectiveness of reforming. The experimental results reveal that the compressive strength of shale specimens subjected to uniaxial compression testing exhibits a dependency on the α within the specimen. The compressive strengths of distinct shale specimens tested under varying bedding angles are presented in Table 1. Figure 12 illustrates a decline in the elastic modulus of the specimens, followed by an increase, as the α is increased. In accordance with the established loading conditions, the compressive strength of the specimen with the α demonstrates a tendency to decrease and then increase. The specimen at the α of 90° and 0° respectively exhibits the maximum compressive strength.

4.2 Simulation of hydraulic fracturing with bedding plane

The 3D discrete lattice method represents a simplified cohesive particle model calculation method based on synthetic rock technology and discrete lattice point theory, which can effectively describe the hydraulic fracture initiation and extension patterns. The method of rock matrix characterization in the synthetic rock mass technique is a flat joint model, and a cohesive particle model is used to simulate rock deformation. The 3D discrete lattice method employs lattice points with masses to supplant particles within the rock matrix. These lattice points are connected with springs of pre-determined strength, which not only streamlines the model of cohesive particles but also markedly increases the number of computable grids and enhances computational efficiency in comparison to the traditional discrete element method.

Based on the 3D discrete lattice method, this paper establishes two true three-dimensional hydro-mechanically coupled fracturing models, each with dimensions of 1 m × 1 m × 1 m, in order to analyze the influence of a bedding plane with a 45° bedding angle on fracturing effectiveness. In this model, the average compressive

TABLE 2 Physical parameters of model matrix.

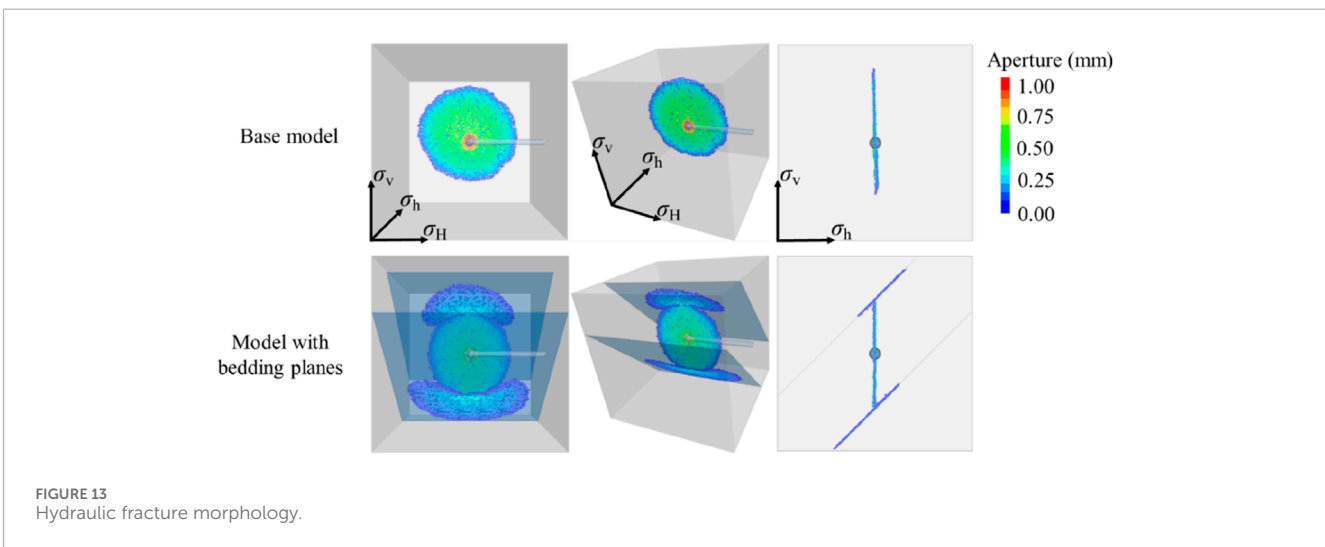| Physical parameters	Vertical stress σ_V (MPa)	Maximum horizontal principal stress σ_H (MPa)	Minimum horizontal principal stress σ_h (MPa)	Uniaxial compressive strength (MPa)
Value	12.00	15.00	7.00	42.20
Physical parameters	Uniaxial tensile stress (MPa)	Elastic modulus (GPa)	Poisson ratio	Fracture toughness (MPa·m0.5)
Value	3.50	1.24	0.25	0.47

FIGURE 13
Hydraulic fracture morphology.
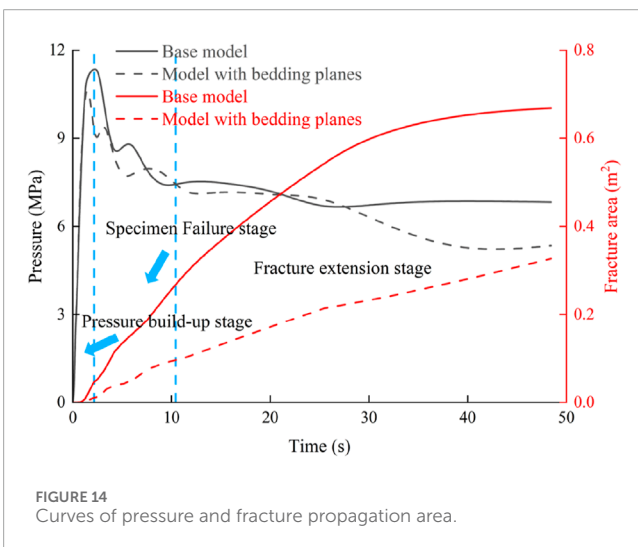
FIGURE 14
Curves of pressure and fracture propagation area.

strength and elastic modulus of the specimen at α of 45° were employed to represent the reservoir matrix. The specific mechanical property parameters are provided in Table 2.

The simulation results illustrate that in the base model, in which the bedding plane is not taken into account, the hydraulic fracture extends in a circular shape in the direction perpendicular to the minimum horizontal principal stress. As seen in Figure 13,

the anisotropic reservoir matrix has an impact on the fracture extension pattern, which is erratic and the upper portion of the fracture is higher than the lower portion. In the model that considers the bedding plane, both the initial expansion direction and the pattern of hydraulic fracture are consistent with those observed in the base model. Bedding planes in shale reservoirs are frequently characterized by defects in the reservoir, which exhibit reduced strength relative to the matrix. These defects tend to exhibit higher porosity. Consequently, during the process of continuous fracturing fluid injection, a substantial volume of fracturing fluid is directly introduced into the bedding plane upon contact with the hydraulic fracture. This interaction prompts the hydraulic fracture to expand in a specific direction. In the ensuing fracturing process, hydraulic fractures extended and activated extensive areas of bedding planes along the upper and lower bedding planes, respectively.

Furthermore, an examination of the cloud diagram depicting fracture morphology reveals that the hydraulic fracture color in the matrix portion of the model comprising bedding planes exhibits a bluish tint. This deviation is attributed to the substantial influx of fracturing fluid into the bedding plane, resulting in a fracture aperture that is comparatively diminished. However, the model containing laminar surfaces demonstrates a 1.96-fold increase in the extent of its hydraulic cracks (Figure 14). Furthermore, Figure 15 elucidates the variation in pressure curve behavior between the two models. It is evident that there is minimal disparity between

the pressure curves of the two models during the pressure build-up stage and the specimen failure stage. However, the pressure profiles in the model containing bedding planes in the subsequent fracture extension stage were significantly lower than those in the baseline model. This phenomenon was attributed to the fact that the mechanical strength of the bedding planes was weaker than that of the matrix. As a result, the fracture was more likely to extend along the bedding planes. In summary, while the presence of bedding planes reduces the aperture of hydraulic fractures, which is unfavorable to the subsequent oil and gas extraction, it also effectively increases the total expansion area of hydraulic fractures, which promotes the fracture modification of the target reservoir. Consequently, leveraging the diminished cementing capacity of the bedding plane to broaden the modification range of hydraulic fracture, while concurrently meticulously delineating the fracturing parameters for defects characterized by diminished fracture aperture, emerges as a pivotal research finding. This approach is instrumental in optimizing the efficiency of fracturing and modification, thereby enhancing the recovery of oil and gas.

5 Conclusion

In order to investigate the impact of varying bedding angles on the mechanical characteristics and failure modes of shale, this study initially conducted uniaxial compression tests under controlled indoor conditions. The physical parameter evolution mechanism of shale under variable bedding angles and the associated damage processes were analyzed. Furthermore, the influence of the bedding plane on hydraulic fracturing was simulated, and the main conclusions of this paper are as follows.

(1) The macro-mechanical parameters of shale under different bedding angles exhibit notable variation. Specimens display a initial decline in compressive strength and modulus of elasticity, followed by an increase with increasing bedding angle. A comparison of the macroscopic damage process and fracture of the rock samples during the experimental process revealed that the highest number of fractures occurred at bedding angles of around 45° and 90°.

(2) At bedding angles of 0°–15°, the predominant damage mode observed in the specimen is a combination of tensile and shear failure across the bedding plane. When the bedding angle of the specimen is 30°–60°, the predominant damage mode is shear damage along the bedding planes. In specimens with bedding angles between 75° and 90°, the predominant damage mode is tensile damage parallel to the bedding plane, accompanied by shear damage along the bedding plane.

(3) The stress-strain curves, plotted based on the uniaxial compression test data, demonstrate that the stress-strain curves of the specimens can be divided into four distinct stages: compaction, elasticity, yielding and damage. In this experiment, all specimens in the compression stage exhibited a sharp increase in the curve, which subsequently reached its maximum load capacity. Following the peak stress, the curve declines in a segmental manner, with a notable change in the overall structure. This results in a rapid decrease in bearing capacity, with some specimens fracturing directly through the entire specimen, leading to a complete loss of bearing capacity.

(4) Upon undertaking a simulation of hydraulic fracture, it was observed that the hydraulic fracture in the base model exhibited a circular expansion pattern along the direction perpendicular to the minimum horizontal principal stress. In the model with bedding planes, the initial expansion direction and pattern of the hydraulic fracture were consistent with those observed in the base model. Subsequently, the hydraulic fractures intersected with the bedding planes, resulting in the formation of semi-circular shaped hydraulic fractures in the upper and lower bedding planes, respectively. Furthermore, the aperture of the hydraulic fracture in the model containing the bedding plane is smaller than that of the base model, and the pressure in the extension stage of the fracture is lower. However, the extension area of the hydraulic fracture within the model containing the bedding plane is larger.

Data availability statement

The original contributions presented in the study are included in the article/supplementary material, further inquiries can be directed to the corresponding author.

Author contributions

Funding

Conflict of interest

Authors XW and QL were employed by Oil & Gas Technology Research Institute of Changqing Oilfield Company. Author JM was employed by PetroChina Xinjiang Oilfield Company. Author MZ was employed by CNPC Offshore Engineering Company Limited.

The remaining authors declare that the research was conducted in the absence of any commercial or financial relationships that could be construed as a potential conflict of interest.

Generative AI statement

The author(s) declare that no Generative AI was used in the creation of this manuscript.

Publisher's note

All claims expressed in this article are solely those of the authors and do not necessarily represent those of their affiliated organizations, or those of the publisher, the editors and the reviewers. Any product that may be evaluated in this article, or claim that may be made by its manufacturer, is not guaranteed or endorsed by the publisher.

References

Fu, H., Huang, L., Hou, B., Weng, D., guan, B., Zhong, T., et al. (2024). Experimental and numerical investigation on interaction mechanism between hydraulic fracture and natural fracture. *Rock Mech. Rock Eng.* 57, 10571–10582. doi:10.1007/s00603-024-04101-3

Gao, M., Yang, M., Lu, Y., Levin, V. A., He, P., and Zhu, H. (2024). Mechanical characterization of uniaxial compression associated with lamination angles in shale. *Adv. Geo-Energy Res.* 13, 56–68. doi:10.46690/ager.2024.07.07

Gu, M. Z., Sheng, M., Zhuang, X. Y., Li, X. Y., and Li, G. S. (2024). The influences of perforating phase and bedding planes on the fracture deflection in laminated shale. *Pet. Sci.* 21, 1221–1230. doi:10.1016/j.petsci.2023.10.015

He, J., Lin, C., Li, X., Zhang, Y., and Chen, Y. (2017). Initiation, propagation, closure and morphology of hydraulic fractures in sandstone cores. *Fuel* 208, 65–70. doi:10.1016/j.fuel.2017.06.080

He, R., Yang, J., Li, L., Yang, Z., Chen, W., Zeng, J., et al. (2023). Investigating the simultaneous fracture propagation from multiple perforation clusters in horizontal wells using 3D block discrete element method. *Front. Earth Sci. (Lausanne)* 11. doi:10.3389/feart.2023.1115054

Huang, L., Dontsov, E., Fu, H., Lei, Y., Weng, D., and Zhang, F. (2022). Hydraulic fracture height growth in layered rocks: perspective from DEM simulation of different propagation regimes. *Int. J. Solids Struct.* 238, 111395. doi:10.1016/j.ijsolstr.2021.111395

Huang, L., He, R., Yang, Z., Tan, P., Chen, W., Li, X., et al. (2023a). Exploring hydraulic fracture behavior in glutenite formation with strong heterogeneity and variable lithology based on DEM simulation. *Eng. Fract. Mech.* 278, 109020. doi:10.1016/j.engfracmech.2022.109020

Huang, L., Liao, X., Fan, M., Wu, S., Tan, P., and Yang, L. (2024a). Experimental and numerical simulation technique for hydraulic fracturing of shale formations. *Adv. Geo-Energy Res.* 13, 83–88. doi:10.46690/ager.2024.08.02

Huang, L., Liao, X., Fu, H., Wang, X., Weng, D., Feng, G., et al. (2025). Interaction behaviors between finite-scale natural and hydraulic fractures in hot dry rock geothermal systems. *Phys. Fluids* 37. doi:10.1063/5.0252814

Huang, L., Liao, X., Fu, H., Zhang, L., Zhao, Y., Wang, X., et al. (2024b). Interplay mechanisms between hydraulic fractures and natural fractures in various propagation regimes. *Phys. Fluids* 36. doi:10.1063/5.0234922

Huang, L., Liu, J., Zhang, F., Dontsov, E., and Damjanac, B. (2019). Exploring the influence of rock inherent heterogeneity and grain size on hydraulic fracturing using discrete element modeling. *Int. J. Solids Struct.* 176–177, 207–220. doi:10.1016/j.ijsolstr.2019.06.018

Huang, L., Liu, J., Zhang, F., Fu, H., Zhu, H., and Damjanac, B. (2020). 3D lattice modeling of hydraulic fracture initiation and near-wellbore propagation for different perforation models. *J. Pet. Sci. Eng.* 191, 107169. doi:10.1016/j.petrol.2020.107169

Huang, L., Tan, J., Fu, H., Liu, J., Chen, X., Liao, X., et al. (2023b). The non-plane initiation and propagation mechanism of multiple hydraulic fractures in tight reservoirs considering stress shadow effects. *Eng. Fract. Mech.* 292, 109570. doi:10.1016/j.engfracmech.2023.109570

Khalili, M., Fahimifar, A., and Shobeiri, H. (2023). The effect of bedding planes on the bending strength of rock-like material and evaluation of the crack propagation mechanism. *Theor. Appl. Fract. Mech.* 127, 104061. doi:10.1016/j.tafmec.2023.104061

Li, M., Zhang, F., Zhuang, L., Zhang, X., and Ranjith, P. (2020). Micromechanical analysis of hydraulic fracturing in the toughness-dominated regime: implications to supercritical carbon dioxide fracturing. doi:10.1007/s10596-019-09925-5/Published

Lin, C., Deng, S., Mao, J., Jiang, Z., Chen, X., Yang, X., et al. (2024a). A new brittleness evaluation index for reservoir rocks based on fuzzy analytic hierarchy process and energy dissipation. *SPE J.* 29, 5272–5285. doi:10.2118/223083-pa

Lin, C., He, J., Li, X., Wan, X., and Zheng, B. (2017). An experimental investigation into the effects of the anisotropy of shale on hydraulic fracture propagation. *Rock Mech. Rock Eng.* 50, 543–554. doi:10.1007/s00603-016-1136-4

Lin, C., Jia, X., Deng, S., Mao, J., Chen, X., He, J., et al. (2024b). The roles of micro pores and minerals in shale during hydraulic fracturing. *Rock Mech. Rock Eng.* 57, 10177–10186. doi:10.1007/s00603-024-04063-6

Liu, H., Jing, H., Yin, Q., Meng, Y., and Zhu, G. (2023). Effect of bedding plane on mechanical properties, failure mode, and crack evolution characteristic of bedded rock-like specimen. *Theor. Appl. Fract. Mech.* 123, 103681. doi:10.1016/j.tafmec.2022.103681

Liu, M., Luo, X., Bi, R., Zhou, J., and Du, K. (2023). Impacts of bedding angle and cementation type of bedding planes on mechanical behavior of thin-layer structured bedded rocks under uniaxial compression. *Geomechanics Energy Environ.* 35, 100473. doi:10.1016/j.gete.2023.100473

Liu, Q., Li, J., Liang, B., Liu, J., Sun, W., He, J., et al. (2023). Complex wettability behavior triggering mechanism on imbibition: a model construction and comparative study based on analysis at multiple scales. *Energy* 275, 127434. doi:10.1016/j.energy.2023.127434

Liu, Y., Yang, H., Zhang, Q., and Xiong, D. (2022). Properties of a shale bedding plane and its influence on the geometric parameters of fracture propagation in volume fracturing. *Eng. Fract. Mech.* 266, 108413. doi:10.1016/j.engfracmech.2022.108413

Luo, H., Xie, J., Huang, L., Wu, J., Shi, X., Bai, Y., et al. (2022). Multiscale sensitivity analysis of hydraulic fracturing parameters based on dimensionless analysis method. *Lithosphere* 2022. doi:10.2113/2022/9708300

Luo, P., Li, D., Zhou, A., Ma, J., Zhu, Q., and Jiang, J. (2023). Influence of bedding plane on the tensile properties and crack propagation of soft and hard laminated rock-like under Brazilian test. *Theor. Appl. Fract. Mech.* 127, 104087. doi:10.1016/j.tafmec.2023.104087

Shao, Y., Kim, J., He, C., Yin, H., Mehrishal, S., Yao, C., et al. (2024). Experimental investigation of the coupled effects of bedding planes and flaws on fracture evolution of soft bedded rocks based on 3D printing and DIC technologies. *Theor. Appl. Fract. Mech.* 133, 104591. doi:10.1016/j.tafmec.2024.104591

Song, R., Liu, J., and Cui, M. (2017). A new method to reconstruct structured mesh model from micro-computed tomography images of porous media and its application. *Int. J. Heat. Mass Transf.* 109, 705–715. doi:10.1016/j.ijheatmasstransfer.2017.02.053

Song, R., Liu, J., Yang, C., and Sun, S. (2022). Study on the multiphase heat and mass transfer mechanism in the dissociation of methane hydrate in reconstructed real-shape porous sediments. *Energy* 254, 124421. doi:10.1016/j.energy.2022.124421

Song, R., Wang, Y., Ishutov, S., Zambrano-Narvaez, G., Hodder, K. J., Chalaturnyk, R. J., et al. (2020). A comprehensive experimental study on mechanical behavior, microstructure and transport properties of 3D-printed rock analogs. *Rock Mech. Rock Eng.* 53, 5745–5765. doi:10.1007/s00603-020-02239-4

Song, Z., Qian, Y., Mao, Y., Chen, X., Ranjith, P. G., and Deng, Q. (2024). Artificial intelligence-based investigation of fault slip induced by stress unloading during geo-energy extraction. *Adv. Geo-Energy Res.* 14, 106–118. doi:10.46690/ager.2024.11.04

Tan, P., Chen, Z., Fu, S., and Zhao, Q. (2023). Experimental investigation on fracture growth for integrated hydraulic fracturing in multiple gas bearing formations. *Geoenergy Sci. Eng.* 231, 212316. doi:10.1016/j.geoen.2023.212316

Tan, P., Chen, Z. W., Huang, L. K., Zhao, Q., and Shao, S. R. (2024). Evaluation of the combined influence of geological layer property and *in-situ* stresses on fracture height growth for layered formations. *Pet. Sci.* 21, 3222–3236. doi:10.1016/j.petsci.2024.07.014

Tan, P., Fu, S., Huang, L., Chen, Z., and Cao, J. (2024c). Effects of orthogonal cleat structures on hydraulic fracture evolution behavior. *Geoenergy Sci. Eng.* 241, 213119. doi:10.1016/j.geoen.2024.213119

Tan, P., Jin, Y., Han, K., Hou, B., Guo, X., Gao, J., et al. (2017). Analysis of hydraulic fracture initiation and vertical propagation behavior in laminated shale formation. *Fuel* 206, 482–493. doi:10.1016/j.fuel.2017.05.033

Tan, P., Jin, Y., and Pang, H. (2021). Hydraulic fracture vertical propagation behavior in transversely isotropic layered shale formation with transition zone using XFEM-based CZM method. *Eng. Fract. Mech.* 248, 107707. doi:10.1016/j.engfracmech.2021.107707

Wu, M., Jiang, C., Song, R., Liu, J., Li, M., Liu, B., et al. (2023). Comparative study on hydraulic fracturing using different discrete fracture network modeling: insight from homogeneous to heterogeneity reservoirs. *Eng. Fract. Mech.* 284, 109274. doi:10.1016/j.engfracmech.2023.109274

Ji, Y., Wang, J., and Huang, L. (2015). Analysis on inflowing of the injecting Water in faulted formation. *Adv. Mech. Eng.* 7, 1–10. doi:10.1177/1687814015590294

Zeng, Q., Bo, L., Li, Q., Sun, J., and Yao, J. (2023). Numerical investigation of hydraulic fracture propagation interacting with bedding planes. *Eng. Fract. Mech.* 291, 109575. doi:10.1016/j.engfracmech.2023.109575

Zhai, M., Xue, L., Bu, F., Yang, B., Huang, X., Liang, N., et al. (2022). Effects of bedding planes on progressive failure of shales under uniaxial compression: insights from acoustic emission characteristics. *Theor. Appl. Fract. Mech.* 119, 103343. doi:10.1016/j.tafmec.2022.103343

Zhang, B., Guo, T., Chen, M., Wang, J., Cao, J., Wang, H., et al. (2024). Effect of bedding planes and property contrast between layers on the propagation mechanism

of hydraulic fracture height in shale reservoirs. *Comput. Geotech.* 175, 106715. doi:10.1016/j.compgeo.2024.106715

Zhang, F., Fang, Y., Elsworth, D., Wang, C., and Yang, X. (2017). Evolution of friction and permeability in a propped fracture under shear. *Geofluids* 2017, 1–13. doi:10.1155/2017/2063747

Zhang, F. S., Huang, L. K., Yang, L., Dontsov, E., Weng, D. W., Liang, H. B., et al. (2022). Numerical investigation on the effect of depletion-induced stress reorientation on infill well hydraulic fracture propagation. *Pet. Sci.* 19, 296–308. doi:10.1016/j.petsci.2021.09.014

Zhang, Y., Guo, T., Chen, M., Qu, Z., Cao, J., Yang, X., et al. (2024). Numerical simulation study of fracture height growth considering the influence of bedding planes. *Comput. Geotech.* 168, 106144. doi:10.1016/j.compgeo.2024.106144

Zhang, Y., Liu, Z., Han, B., Zhu, S., and Zhang, X. (2022). Numerical study of hydraulic fracture propagation in inherently laminated rocks accounting for bedding plane properties. *J. Pet. Sci. Eng.* 210, 109798. doi:10.1016/j.petrol.2021.109798

Zhao, Y., Sun, Z., Gao, Y., Wang, X., and Song, H. (2022). Influence of bedding planes on fracture characteristics of coal under mode II loading. *Theor. Appl. Fract. Mech.* 117, 103131. doi:10.1016/j.tafmec.2021.103131

Zheng, Y., He, R., Huang, L., Bai, Y., Wang, C., Chen, W., et al. (2022). Exploring the effect of engineering parameters on the penetration of hydraulic fractures through bedding planes in different propagation regimes. *Comput. Geotech.* 146, 104736. doi:10.1016/j.compgeo.2022.104736